Simulation of Stratospheric N2O in the NCAR CCM2: Comparison with CLAES Data and Global Budget Analyses

WILLIAM J. RANDEL, BYRON A. BOVILLE, JOHN C. GILLE, PAUL L. BAILEY, AND STEVEN T. MASSIE

National Center for Atmospheric Research, * *Boulder, Colorado*

J. B. KUMER, J. L. MERGENTHALER, AND A. E. ROCHE

Lockheed Palo Alto Research Laboratory, Palo Alto, California

(Manuscript received 21 March 1994, in final form 23 June 1994)

ABSTRACT

Global variability and budgets of stratospheric nitrous oxide (N_2O) are studied using output from a stratospheric version of the NCAR Community Climate Model. The model extends over 0–80 km, incorporating an N_2O-like tracer with tropospheric source and upper-stratospheric photochemical sink, the latter parameterized using linear damping rates obtained from detailed two-dimensional model calculations. Results from the model over several seasonal cycles are compared with observations of N_2O from the Cryogenic Limb Array Etalon Spectrometer instrument on the *Upper Atmosphere Research Satellite*. The model produces N_2O structure and variability that is in reasonable agreement with the observations. Global budgets of stratospheric N_2O are furthermore analyzed using model output, based on the transformed Eulerian-mean, zonal-mean framework. These budgets are used to quantify the importance of planetary wave constituent transport in the stratosphere, for both slow seasonal variations and fast planetary wave events. These results demonstrate that such wave fluxes act to form and sharpen the strong subtropical N_2O gradients observed in satellite measurements.

1. Introduction

Nitrous oxide (N_2O) is an important constituent in the stratosphere for several reasons. It is the primary source of nitrogen-containing compounds in the stratosphere, and these are in turn central for the chemistry of stratospheric ozone. Nitrous oxide has its source in the troposphere, is transported into the stratosphere in the Tropics, and is photochemically destroyed above 30 km. The photochemical lifetime of N_2O below 40 km is >100 days, so that the stratospheric distribution is determined mainly by the circulation; as a consequence, N_2O is a valuable tracer of stratospheric fluid motions. For this reason, N_2O is often used as a conservative tracer in aircraft or satellite data studies of the stratosphere (Hartmann et al. 1989; Schoeberl et al. 1992; Strahan and Mahlman 1994; Manney et al. 1994). Furthermore, the overall characteristics of N_2O are similar to other constituents with tropospheric

sources and stratospheric photochemical sinks (notably CH_4, CF_2Cl_2, and $CFCl_3$), so that a detailed understanding of N_2O is implicitly tied to the budgets of these other constituents as well. The importance of understanding stratospheric N_2O has been recognized and its global budget analyzed in a series of pioneering general circulation model (GCM) studies by Mahlman and coworkers (e.g., Mahlman et al. 1980; Mahlman et al. 1986; Mahlman and Umscheid 1987). The results of their simulations show basic agreement with satellite measurements of N_2O from the Stratospheric and Mesospheric Sounder (SAMS) (Jones and Pyle 1984) and with aircraft measurements of N_2O (Strahan and Mahlman 1994). The SAMS N_2O (and CH_4) observations have also been utilized for determining the mean transport circulation in the stratosphere (Solomon et al. 1986; Holton and Choi 1988; Stanford et al. 1993). The ability to correctly simulate N_2O is now used as a benchmark for two-dimensional models of the middle atmosphere (Prather and Remsberg 1992; Garcia et al. 1992).

The focus of this present work is an analysis of the variability and budgets of stratospheric N_2O as simulated in a recent stratospheric version of the NCAR Community Climate Model (CCM2). This model incorporates an N_2O-like tracer with sources in the troposphere and parameterized photochemical sinks in the stratosphere. We compare the simulated N_2O behavior

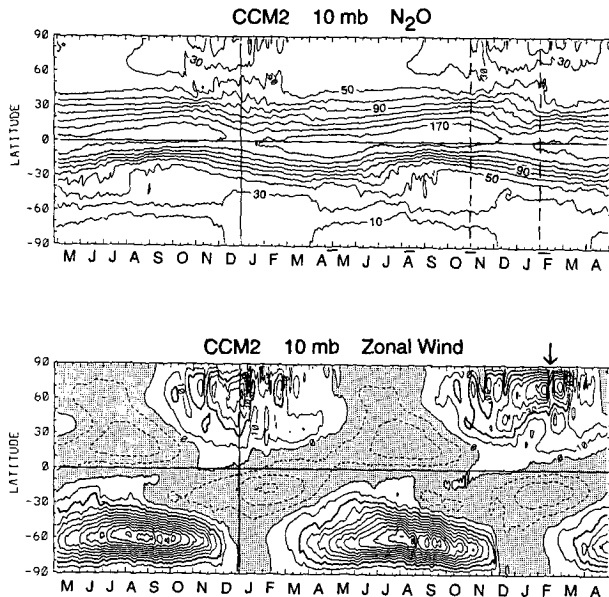CCM2   10 mb   N₂O

CCM2   10 mb   Zonal Wind

FIG. 1. Latitude–time diagrams of 10-mb zonal-mean N_2O mixing ratio (top; units of ppbv) and zonal-mean zonal wind (bottom; units of m s^{-1}) from two years of the CCM2 simulation. Dashed lines in the top panel bracket the time period analyzed in the budget calculations, and the arrow above the lower panel highlights the stratospheric warming event analyzed in section 4b.

to recent observations of N_2O from the Cryogenic Limb Array Etalon Spectrometer (CLAES) instrument on the *Upper Atmosphere Research Satellite (UARS)*. These observations cover 16 months (January 1992–April 1993), and we compare observed and simulated N_2O structure and seasonal variation throughout the stratosphere. We furthermore use the model output to study the budget of zonal-mean N_2O in the stratosphere. The focus here is to determine the relative importance and balance of individual terms in the transformed Eulerian-mean tracer continuity equation. These budgets are evaluated for slow seasonal variations and for shorter-term variability associated with winter hemisphere planetary wave events.

2. Model and observed data

a. CCM2

The model results shown here are based on a stratospheric version of CCM2, with a domain covering 0–80 km. Details of CCM2 and its stratospheric dynamical climatology over several years are shown in Boville (1994). The simulation here is based on T42 horizontal spectral resolution (approximately 2.8 degrees latitude–longitude), with a vertical resolution of 1.5–2 km in the stratosphere. An N_2O-like tracer χ is included in this simulation, with a constant tropospheric mixing ratio of 300 parts per billion by volume (ppbv) and a parameterized photochemical sink term of the form

$$\frac{\partial \chi}{\partial t} = - \frac{\chi}{\tau(y, z, t)}.$$

Here τ is a linearized destruction timescale obtained from the two-dimensional simulation of Garcia and Solomon (1983) [τ for January is shown in Fig. 1 of Solomon et al. (1986)]. Interpolated monthly mean values of τ (as function of latitude and height) are used in this simulation. The initial conditions for N_2O were specified from the two-dimensional model results, and a 10-yr integration was performed; the results shown here are from the final two years of that simulation.

Although CCM2 simulation of the Northern Hemisphere (NH) winter stratospheric circulation is in reasonable agreement with observations, the Southern Hemisphere (SH) winter circulation suffers from the common "cold pole" bias, wherein the SH polar vortex is too strong and persists too long into spring. This bias is probably related to an insufficient amount of gravity wave drag in the model SH stratosphere and mesosphere, and this is in turn associated with a weakened residual mean circulation during SH winter (Garcia and Boville 1994). In terms of the simulated N_2O structure, one would anticipate Antarctic vortex N_2O values biased somewhat high and tropical values somewhat low in this simulation during SH winter, due to this decreased mean meridional circulation. A further apparent defeat in this simulation is a weakened semiannual oscillation (SAO) in the tropical upper stratosphere compared with observations (Boville 1994; Sassi et al. 1993); this is also likely due to weak gravity wave driving in the model (Tropics). This results in a weakened model downward velocity in the tropical upper stratosphere during the westerly (equinox) phase of the SAO, and the absence of a pronounced double-peaked structure in the model tracer field [as observed in SAMS N_2O observations (Jones and Pyle 1984; see also below)].

b. CLAES data

Details of the CLAES instrument on *UARS* are described in Kumer et al. (1993). The detailed structure of the CLAES constituent data changes as improvements in data reduction are implemented; the results here are based on data Version 6 (V6). Vertical resolution is approximately 2.5 km over 20–55 km. CLAES V6 data are available from 9 January 1992 until its solid cryogen was expended on 6 May 1993. The *UARS* satellite yaws at intervals of approximately one month, providing coverage from approximately 30° in one hemisphere to 80° in the other for successive periods. Orbiting satellite data were mapped using a Kalman filter technique, providing an estimate of the zonal mean and six zonal wave components once per day, with a latitude resolution of 4 degrees.

The quality of the CLAES V6 N_2O data is discussed in Gille and Grose (1994), based on correlative data

comparisons. The mean difference between CLAES and correlative N_2O data is approximately 10%–25% over the altitude range 22–50 km studied here. Precision (repeatability) estimates based on orbit-to-orbit comparisons are in the 10%–20% range (J. C. Gille and L. V. Lyjak 1994, personal communication); the mapped data used here will have even smaller values for the precision, or random errors. A major uncertainty is in the systematic errors, which appear to vary with altitude, latitude, and time. Two particular problems evident in these data are the appearance of isolated maxima in vertical profiles ("spikes") and excessive vertical gradients in the lower stratosphere. To remove these short vertical wavelength features, we have smoothed these data in the vertical with two passes of a running 1–1–1 filter, and we focus on qualitative aspects of the data in the middle and upper stratosphere. The general agreement of these data with the correlative data, and similarly for comparisons with N_2O measurements from the Improved Stratospheric and Mesospheric Sounder (ISAMS) on UARS (Gille and Grose 1994), suggest that the overall distributions shown here are certainly qualitatively, and roughly quantitatively, correct.

3. Model–CLAES N_2O comparisons

Figure 1 shows time evolution of model zonal-mean N_2O (hereafter referred to as $\bar{\chi}$) at 10 mb throughout two seasonal cycles, together with the 10-mb zonal-mean zonal wind (included to illustrate dynamical variability). In the figure, $\bar{\chi}$ exhibits a maximum near the equator, with strong latitudinal gradients in the subtropics of both hemispheres. The tropical $\bar{\chi}$ maximum is centered somewhat north of the equator during SH winter–spring (near 10°N), moving back over the equator or slightly south during NH winter–spring. The subtropical gradient region undergoes a transition period during winter in each hemisphere, such that the gradients are tightened and move to lower latitudes (toward the summer hemisphere); this is particularly clear in both SH winters in Fig. 1, and also the second NH winter. The first NH winter in Fig. 1 was more dynamically disturbed than the second during January–February (compare the zonal wind structure in Fig. 1), and tight subtropical $\bar{\chi}$ gradients are not seen in late spring during that first year.

Figure 2a shows a similar diagram of CLAES zonal-mean N_2O at 10 mb, covering January 1992–April 1993. As discussed in section 2, CLAES data are not available between approximately 30° and the pole for alternating yaw periods (and for a few periods when spacecraft problems caused CLAES to be turned off), and these periods of missing data are indicated by the shaded regions in Fig. 2a (although smoothly interpolated values are provided by the mapping routine, and included in Fig. 2a). Figure 2b shows the zonal-mean zonal wind over this time period, derived from National
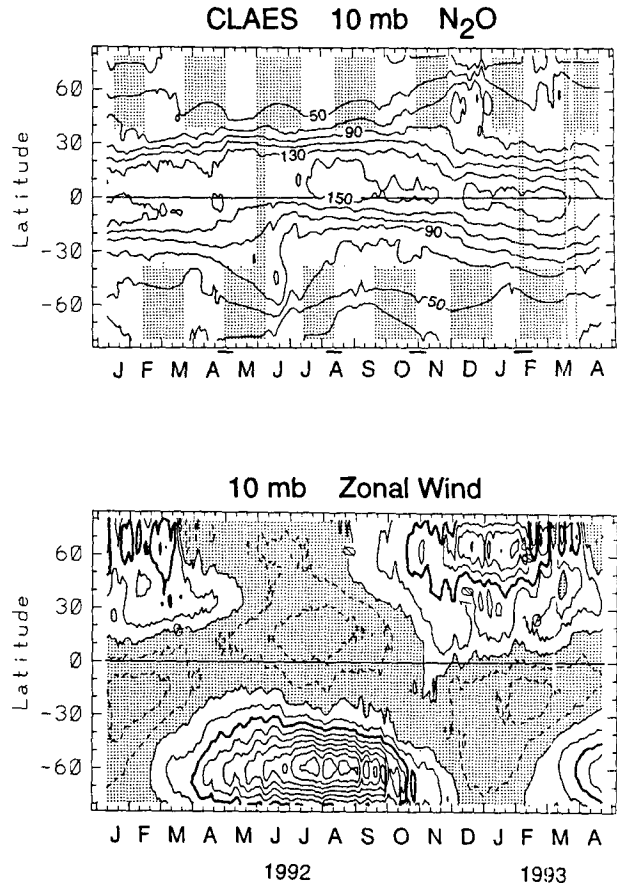

FIG. 2. Latitude–time diagrams of 10-mb zonal-mean N_2O mixing ratio obtained from CLAES measurements (top; units of ppbv) and zonal-mean zonal wind derived from NMC data (bottom; units of m s^{-1}). These data cover January 1992–April 1993. Shaded regions in the upper panel denote periods where CLAES data are unavailable, and the bars below the lower axis denote the time periods for which zonal-mean cross sections are shown in Fig. 6.

Meteorological Center (NMC) stratospheric geopotential height analyses; these data may be directly compared with the final 16 months of model simulation shown in Fig. 1. The overall structure and variability of the observed and modeled $\bar{\chi}$ are similar—notably 1) tropical maximum north of the equator in SH winter and over the equator in NH winter, 2) rapid movement toward the equator of the subtropical gradient region in early–middle winter, and 3) substantial variability in $\bar{\chi}$ in winter midlatitudes prior to this transition time; in late winter–spring the $\bar{\chi}$ fields are relatively quiet. The northward shift of the tropical maximum occurs later in the model (June–July) than in the observations (March–May), and the observed low-latitude maximum protrudes more strongly into the NH summer stratosphere than that in the model. Both of these differences are consistent with the reduced mean meridional circulation in the model during SH winter (as discussed in section 2a above). The model shows some

degree of interannual variability in the southward iso-line shift during NH winter (compare the two NH winters in Fig. 1), and this makes detailed comparison with the single year of CLAES data indecisive.

Figures 3–4 show corresponding plots of $\bar{\chi}$ at 2.2 mb from the model and observations, and at this level there are more notable differences. Namely, the observed $\bar{\chi}$ shows substantial minima in the Tropics during solstice seasons (relative seasonal variations of order 100%), compared to approximate 25% variations in the model (although the temporal phasing is approximately correct). This amplitude difference is likely attributable to the weakened tropical SAO circulation in the model, discussed in section 2a above. This symptom could also be attributable to the parameterized photochemical relaxation in the model upper stratosphere being too weak.

Figures 5–6 show meridional cross sections of modeled and observed $\bar{\chi}$ throughout the seasonal cycle. The observed data are sampled over approximate two-week time periods straddling satellite yaw intervals (these periods are denoted in Figs. 2–4), so that approximately one week of data is sampled from high latitudes of each hemisphere over these times. The model data in Fig. 5 are simple two-week averages over the same corresponding time periods (indicated in Figs. 1–3). The broad background structure and seasonal evolution of the simulated and observed fields are similar, with some notable differences. The simulated tropical maximum is more pronounced (sharper subtropical gradients) than those observed after equinox (April–May and October–November). This may be partly due to the weakened upper-stratospheric tropical SAO circulation in the model, as noted above. Note that the CLAES data do show evidence of weak double-peaked structure about the equator in the upper stratosphere during the equinoxes, which is absent in the model. The double-peaked structure in the observations is somewhat stronger for the first cycle of the year (April–May in Fig. 6; see also the April 1993 data in Fig. 4), and this is a well-known feature of the SAO (Holton and Choi 1988; see also Dunkerton and Delisi 1988).

A well-defined SH polar vortex is identified in the model in August and October–November, with de-
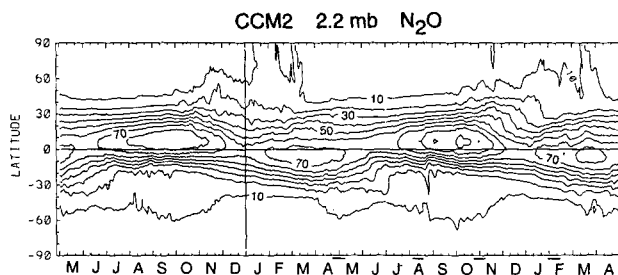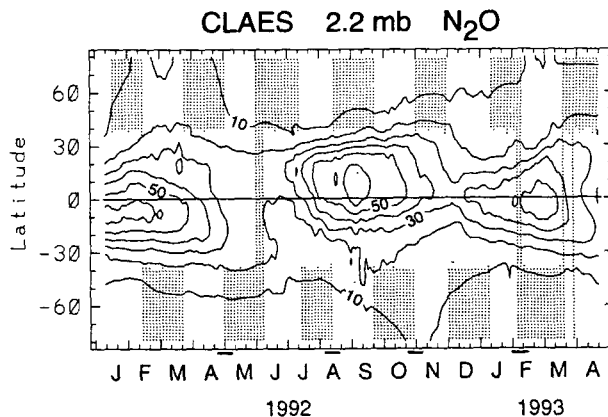
FIG. 4. Latitude–time variation of zonal-mean N_2O (ppbv) at 2.2 mb obtained from CLAES measurements. Shaded regions denote periods where CLAES data are unavailable.

pleted tracer mixing ratios poleward of 60°S [similar to the constituent observations in Russell et al. (1993)]. Flattened isolines in SH midlatitudes at these times identify the surf zone region, and near–mirror image patterns are found in the model NH in January–February [although this time sample (from the second model year shown in Fig. 1) is from a relatively undisturbed period; zonal averages from other NH winter time samples from the model do not show such a clear vortex–surf zone structure].

The CLAES data in Fig. 6 show a clear SH vortex–surf zone structure in August and depleted polar mixing ratios in October–November. The January–February zonal-mean CLAES data do not exhibit this structure, but this is mainly due to a displacement of the vortex far off the pole at this time (see Fig. 2 of Manney et al. 1994).

4. Model budget analysis

The overall consistent agreement between modeled and observed N_2O structure shown above lends confidence to the N_2O simulation, particularly for the largest-scale features. This prompts further analysis of the model simulation, in particular budget analyses to determine the relative importance and balances of individual terms in the zonal-mean tendency equations. The utility of using model output for such diagnoses is that accurate budgets can be obtained, whereas similar calculations performed on observed data can be plagued by large imbalances.

The budget calculations presented here are based on the transformed Eulerian-mean (TEM) conservation equation for zonal-mean mixing ratio $\bar{\chi}$ [from Andrews et al. (1987), Eq. (9.4.13)]:

FIG. 3. Latitude–time diagram of zonal-mean N_2O (ppbv) at 2.2 mb from the CCM2 simulation.

$$\frac{\partial \bar{\chi}}{\partial t} = -\overline{v}^* \bar{\chi}_y - \overline{w}^* \bar{\chi}_z + \bar{S} + \frac{1}{\rho} \nabla \cdot \mathbf{M}. \qquad (1)$$
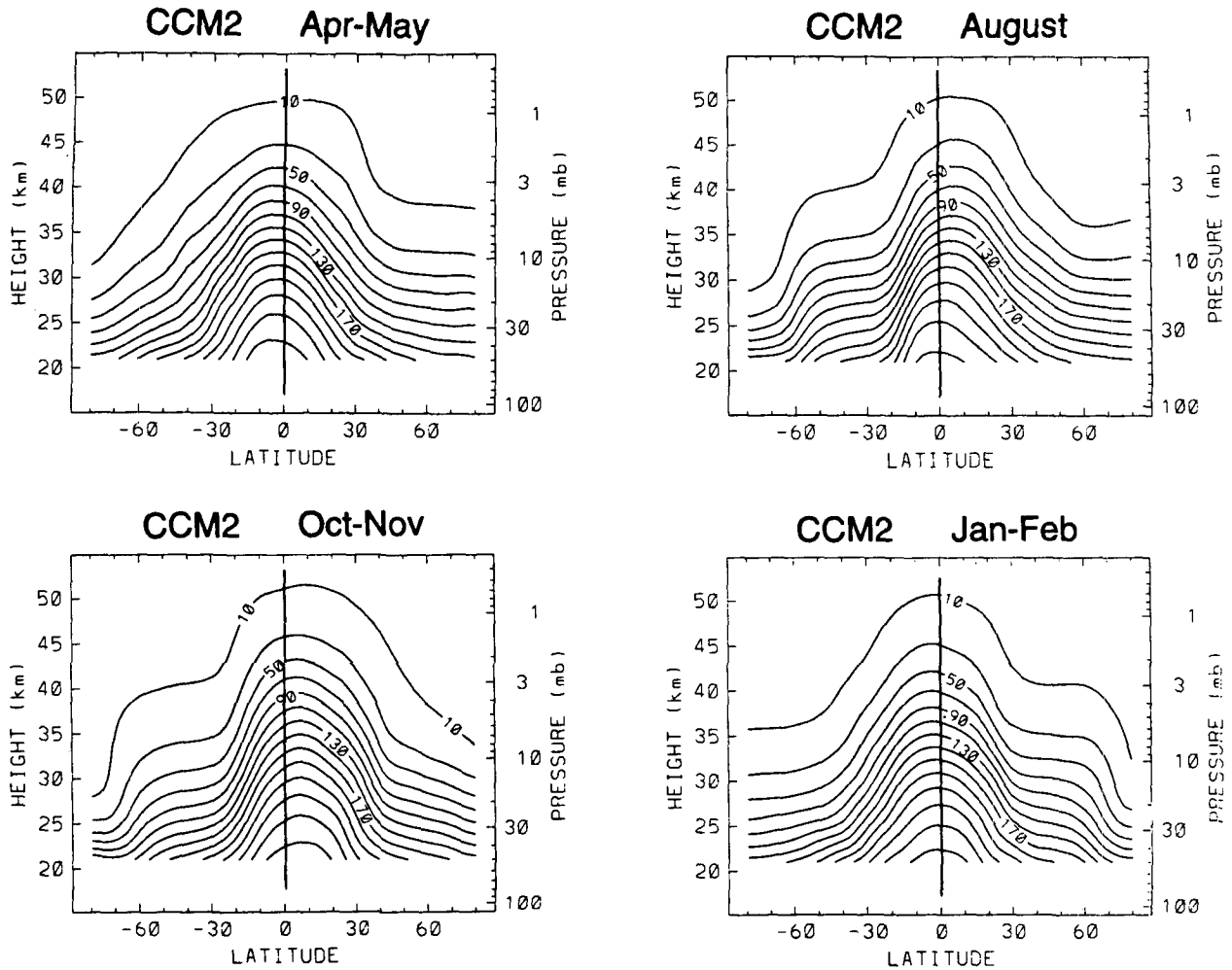
FIG. 5. Seasonal variation of zonal-mean N_2O (ppbv) taken from the CCM2 simulation.

Here $\overline{v^*}$ and $\overline{w^*}$ are components of the residual mean meridional circulation:

$$\overline{v^*} = \overline{v} - \frac{1}{\rho}\frac{\partial}{\partial z}\left(\rho\,\frac{R}{H}\,\frac{\overline{v'T'}}{N^2}\right) \qquad (2a)$$

$$\overline{w^*} = \overline{w} + \frac{1}{a\cos\phi}\frac{\partial}{\partial\phi}\left(\cos\phi\,\frac{R}{H}\,\frac{\overline{v'T'}}{N^2}\right), \qquad (2b)$$

where $\overline{S}$ is a zonal-mean source or sink term (the parameterized photochemical sink here), and $\rho^{-1}\nabla\cdot\mathbf{M}$ is an eddy forcing term. The eddy flux vector $\mathbf{M}$ has components

$$M_y = -\rho\left(\overline{v'\chi'} - \frac{R}{H}\,\frac{\overline{v'T'}}{N^2}\,\overline{\chi}_z\right) \qquad (3a)$$

$$M_z = -\rho\left(\overline{w'\chi'} + \frac{R}{H}\,\frac{\overline{v'T'}}{N^2}\,\overline{\chi}_y\right). \qquad (3b)$$

Here overbars denote zonal means and primes devia-

tions therefrom, and other notation is standard. Our calculations use zonal covariances calculated spectrally and simple finite-difference approximations in latitude, height, and time. Time sampling is once daily, with the individual model fields archived as daily averages. These numerical approximations (including prior interpolation of the model data to pressure surfaces) and possible sampling biases (absence of higher frequencies) are potential sources of error in the budget of terms in Eq. (1). However, we find relatively small residuals in our calculations, which suggests that these sources of inaccuracy are minor.

a. Seasonal budgets

Our calculations focus on two timescales of variation seen in Fig. 1: slow seasonal changes, and more rapid daily variability associated with planetary wave events. Seasonal variability is examined for early–middle NH winter of the second model year shown in Fig. 1 (the time period between the dashed lines). During this time
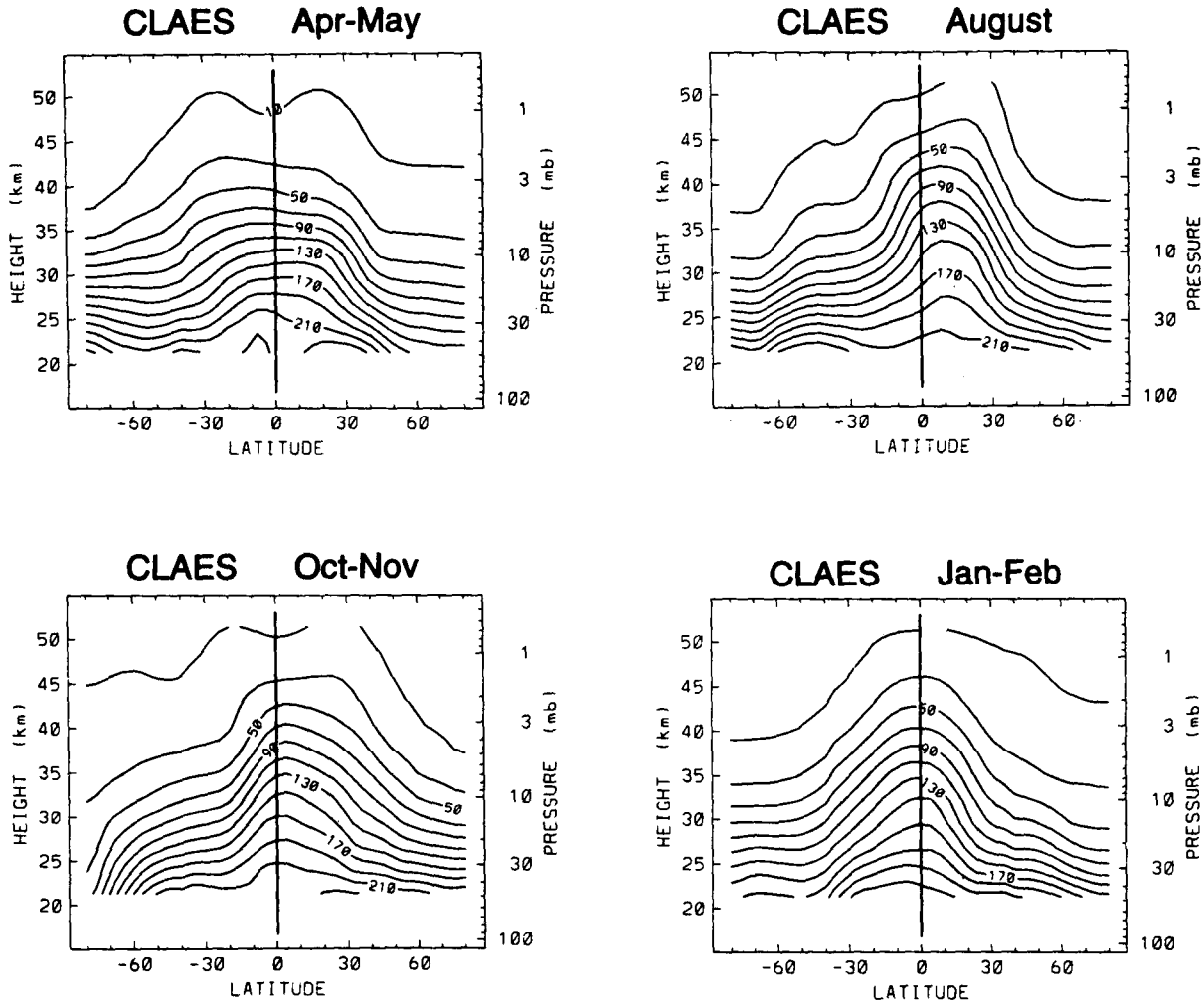
CLAES   Apr-May

CLAES   August

CLAES   Oct-Nov

CLAES   Jan-Feb

FIG. 6. Seasonal variation of zonal-mean N_2O (ppbv) obtained from CLAES data. These averages are sampled over 2-week time periods, as indicated in Figs. 2 and 4.

the low-latitude $\bar{\chi}$ contours move southward and tighten in the NH subtropics. Figure 7 shows meridional cross sections of $\bar{\chi}$ at the beginning and end of this period, together with their difference (i.e., the time-averaged tendency $\partial\bar{\chi}/\partial t$ over this period). Note the vortex–surf zone structure in $\bar{\chi}$ existing in the SH on 1 November, and similarly found in the NH on 31 January; this time period thus covers the breakdown of the model SH vortex and subsequent buildup of the NH vortex.

Figure 8 shows meridional cross sections of the time average of each of the individual terms on the right-hand side of Eq. (1), together with their sum (i.e., the total calculated tendency). The time-average tendencies calculated from the rhs of (1) (Fig. 8) and from the lhs of (1) (Fig. 7) are in reasonable overall agreement in both spatial structure and magnitude, demonstrating the approximate balance in this calculation. The residual (not shown) is a small term in the budget

over most of the model domain, although it is relatively large in the NH subtropics near 30°N (where the other calculated terms are relatively small).

Comparison of the individual terms in Eq. (1) (Fig. 8) shows an overall balance between advection by the residual mean circulation ($-\overline{v^*\bar{\chi}_y} - \overline{w^*\bar{\chi}_z}$) and wave transport effects ($1/\rho\nabla \cdot \mathbf{M}$), with the photochemical damping term ($\bar{S}$) important in the Tropics over 30–50 km. The residual mean circulation ($\overline{v^*}, \overline{w^*}$) calculated from the model (shown in Fig. 8) is in agreement with estimates from observed data (e.g., Gille et al. 1987). The southward seasonal movement of the tropical $\bar{\chi}$ maximum in the model results from mean rising motion in the SH subtropics coupled with strong eddy flux convergence in the NH subtropics (note the mean meridional velocity acts to move the tropical $\bar{\chi}$ contours northward, opposite to the observed changes over this period). The convergence of winter stratosphere wave fluxes are primarily responsible for
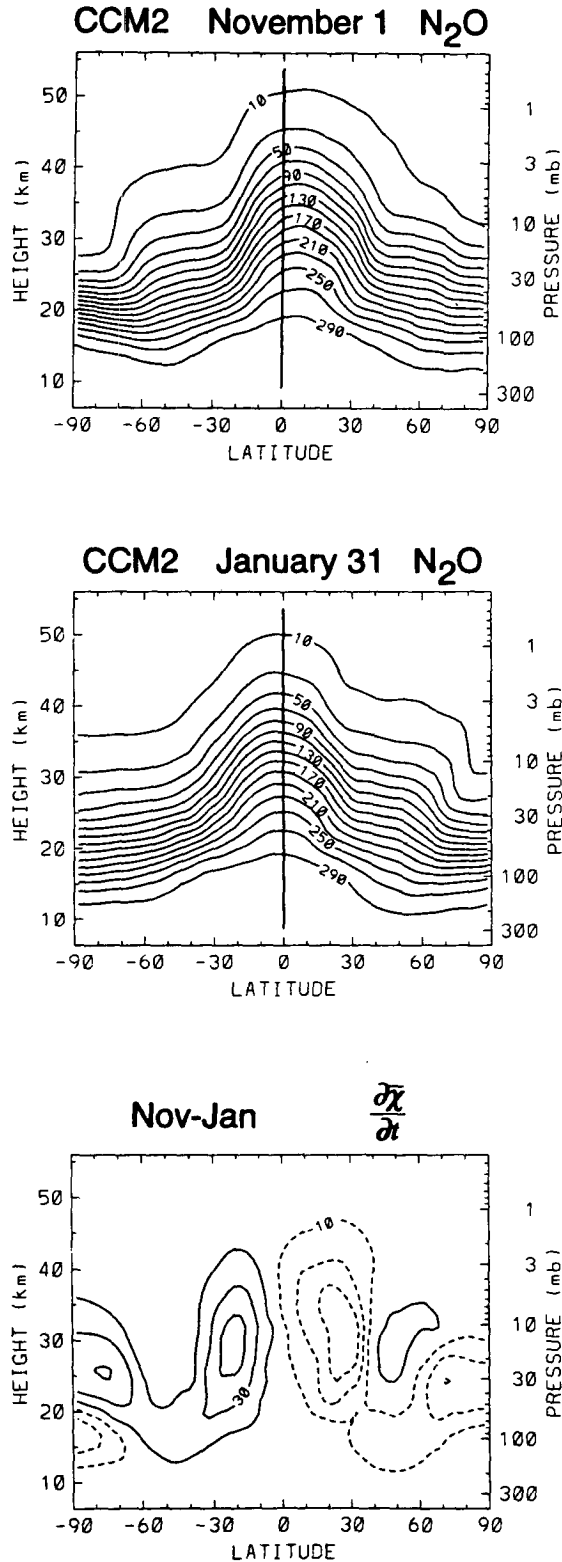
CCM2 November 1 N₂O

CCM2 January 31 N₂O

Nov-Jan $\frac{\partial \overline{\chi}}{\partial t}$

FIG. 7. Zonal-mean N₂O mixing ratios (ppbv) from the CCM2 simulation on 1 November (top) and 31 January (middle); these times are denoted by the dashed lines in the top panel of Fig. 1. Bottom panel shows the mixing ratio difference between these dates; contours are ±10, 30, 50 ppbv 100 days⁻¹.

"sharpening" the subtropical NH $\overline{\chi}$ gradients; note that wave transport effects reach all the way to the equator in Fig. 8. Lowered $\overline{\chi}$ values inside the NH vortex result primarily from the downward mean circulation, although the observed $\overline{\chi}$ change is a relatively small residual between the mean flow and eddy terms. Furthermore, the breakdown of the SH vortex ("filling in" of the low polar $\overline{\chi}$ values over 20–35 km seen on 1 November in Fig. 7) occurs primarily due to wave transport effects.

Included in the diagram showing the eddy divergence tendency in Fig. 8 are vectors representing the local M_y and M_z components; this figure shows the direction and magnitude of eddy tracer fluxes and their divergence, analogous to Eliassen-Palm (E-P) flux cross sections (Edmon et al. 1980). [For clarity in plotting these vectors, we have omitted the density factor in Eq. (3) and multiplied the vertical component of M by a factor of 150, so that M_y and M_z are plotted isotropically in the latitude–height plane.] The M vectors in Fig. 8 show that the eddy forcing is attributable almost entirely to the horizontal flux component, with strong equatorward flux throughout the NH stratosphere, and similarly in the SH lower stratosphere, producing north–south dipole patterns in the induced tendencies. Figure 9 shows the two separate terms that compose M_y [Eq. (3a)]. The first term $(\overline{-v'\chi'})$, the negative of the Eulerian-mean flux) exhibits a dipole pattern in the winter stratosphere, with negative flux in subtropics and positive flux in high latitudes. The second term $((R/H)(\overline{v'T'}/N^2)\overline{\chi}_z)$ is negative in high latitudes and larger than the Eulerian-mean flux, so that the total TEM flux is negative (equatorward). Space–time spectral analyses of these eddy covariances (not shown here) reveal that quasi-stationary or slowly moving planetary-scale waves (zonal wavenumbers 1–3) are primarily responsible for the eddy tracer transport throughout the 15–40-km region highlighted in Fig. 9. The relative smallness of the M_z component in these results (see Fig. 8) is due to the fact that the two terms in M_z [Eq. (3b)] nearly exactly cancel each other (not shown here); this cancellation is a natural consequence of the TEM formalism.

b. Fast timescale variability

Significant day-to-day variability in $\overline{\chi}$ is observed throughout the winter stratosphere (see Fig. 1), and the TEM budget calculations are also well balanced for such high-frequency variations. Figure 10 shows a meridional cross section of the correlation between the daily $\partial\overline{\chi}/\partial t$ and that calculated from Eq. (1) over November–March [daily $\partial\overline{\chi}/\partial t$ calculated from finite differenced $\overline{\chi}$, hereafter called "actual" tendencies, and calculated tendencies are the sum of the right-hand terms in Eq. (1)]. Strong correlation (>0.8) is found throughout extratropics of both hemispheres, with somewhat lower values in the Tropics. These lower
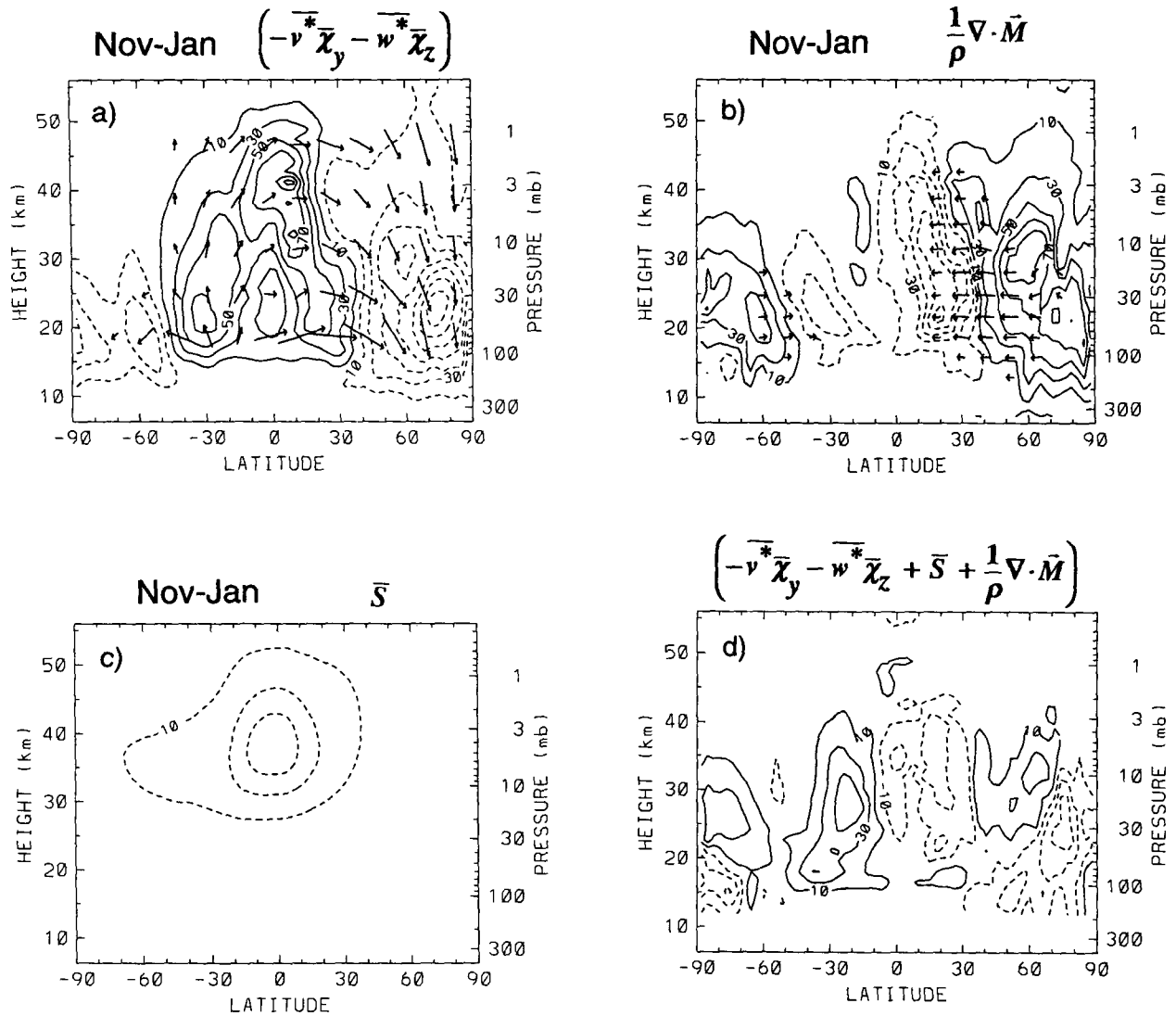
FIG. 8. Individual terms in the time-averaged tracer continuity equation [Eq. (1)] from the model. (a) Residual mean circulation tendency, with arrows indicating residual mean circulation v^*, w^* (for clarity, these arrows have been scaled with the square root of density); (b) eddy flux divergence tendency, with arrows indicating local M-vector components (as discussed in text); (c) parameterized photochemical tendency; (d) sum of the calculated tendencies (compare to actual tendency in Fig. 7). Units in all panels are ppbv 100 days^{-1}.

tropical correlations are due to high-frequency (daily) variations in the calculated terms, which are not echoed in the tendencies estimated from daily data; this suggests that these reduced correlations are related to some aspect of time sampling, and these are not discussed further here.

Figure 11a shows time series of actual and calculated tendencies over the entire NH winter at 50 mb, 60°N, and Fig. 11b shows the individual components of the calculated forcing [from Eq. (1)]. The balance of the daily budget at this location (and over most of the winter stratosphere) is $\partial \bar{\chi} / \partial t \approx -\overline{w^* \bar{\chi}_z} + \rho^{-1} \nabla \cdot \mathbf{M}$, with the actual tendency following patterns of the wave driving, and the mean flow advection tendency having op-

posite sign to the eddy term—that is, these terms cancel to some degree. Note that the wave and mean flow variations are episodic and that the wave effects are to a large degree reversible during individual wave events (positive tendencies followed by negative ones, and vice versa); the net tendency is a small residual of these fluctuations. Figure 11a includes a line showing the running time average of the calculated tendency (calculated using a moving monthly Gaussian smoother, and multiplied by a factor of 10 for clarity), and this shows a net negative tendency at this location during NH winter. Figure 12 shows cross sections of residual circulation tendency and wave flux divergence for consecutive phases of a particular wave (stratospheric
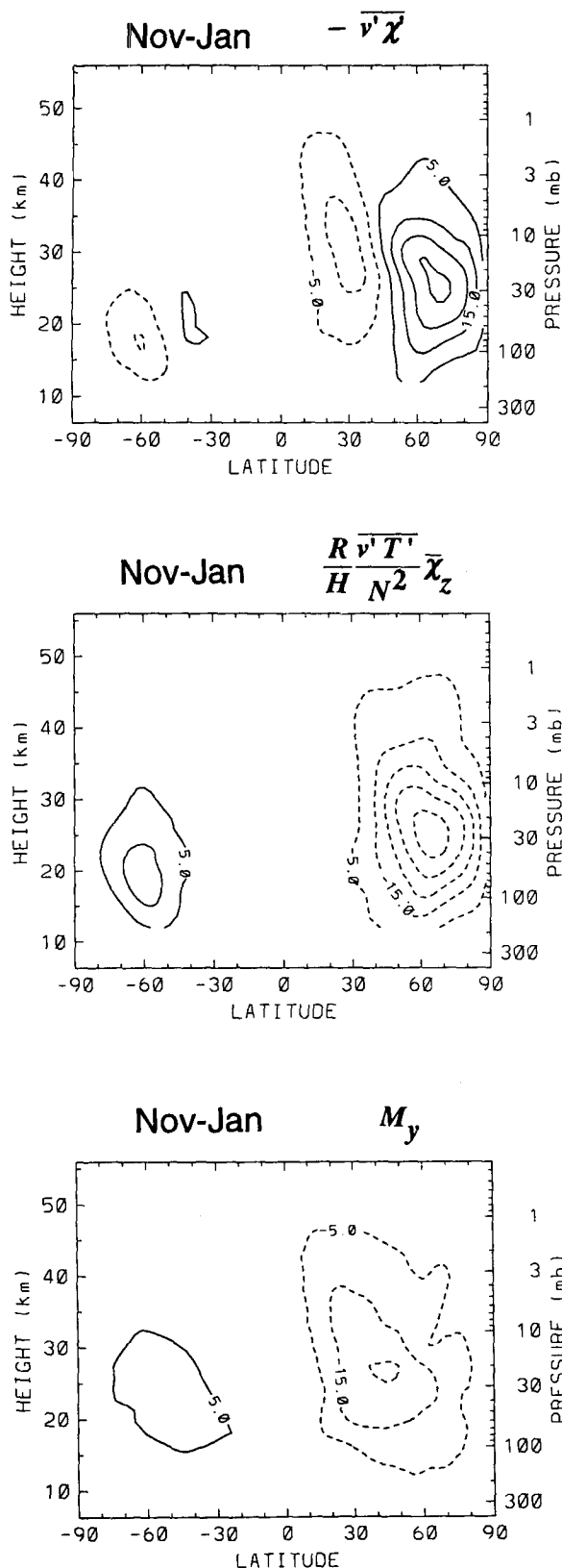
Nov-Jan $\quad -\overline{v'\chi'}$
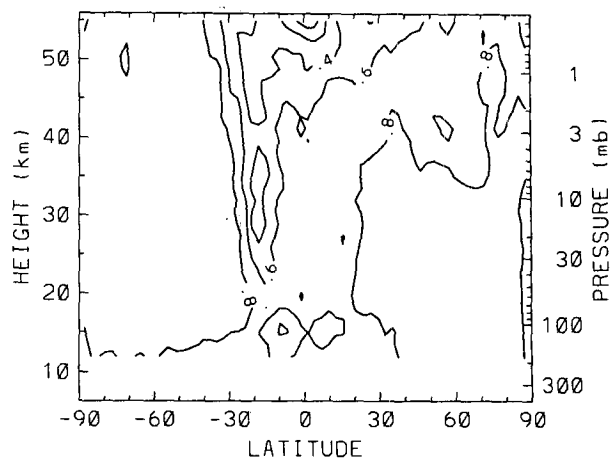

Calculated vs. actual tendency

FIG. 10. Meridional cross section of the correlation between calculated and actual zonal-mean N_2O tendencies [the left- and right-hand sides of Eq. (1)], from model data sampled once daily over November–March.

Nov-Jan $\quad \dfrac{R}{H}\dfrac{\overline{v'T'}}{N^2}\overline{\chi}_z$

warming) event in the model (noted with the arrow in Fig. 1), together with the corresponding E–P flux diagrams to illustrate dynamical aspects of this wave life cycle. The first phase (left-hand panels in Fig. 12)
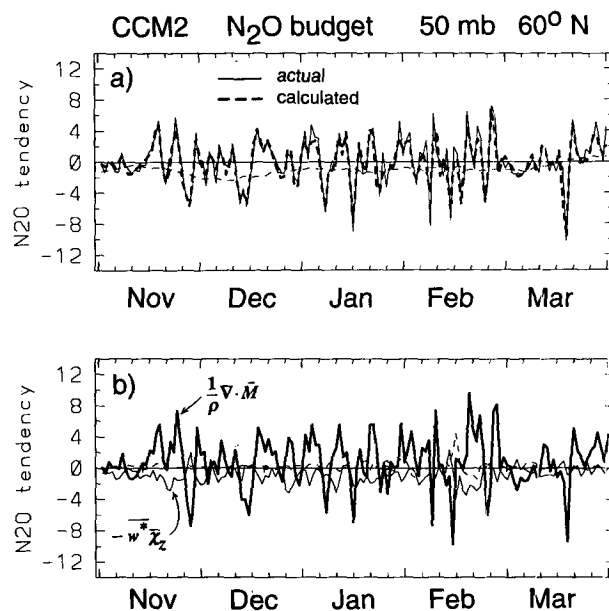
Nov-Jan $\quad M_y$

FIG. 9. Time-averaged components of M_y [Eq. (3a)] from the model, along with their total (lower panel). Units are ppbv per m s^{-1}.

CCM2 N$_2$O budget 50 mb 60° N

FIG. 11. Daily variation of individual terms in the model zonal-mean N_2O budget at 50 mb, 60°N over November–March. Top panel shows actual and calculated tendencies [left- and right-hand sides of Eq. (1)]. Light dashed line is the calculated tendency smoothed in time with a running monthly Gaussian filter, with values multiplied by a factor of 10 for clarity. Lower panel shows the individual forcing terms ($-v^*\overline{\chi}_y$ and S are too small to be clearly seen at this position). Units are ppbv day^{-1}.
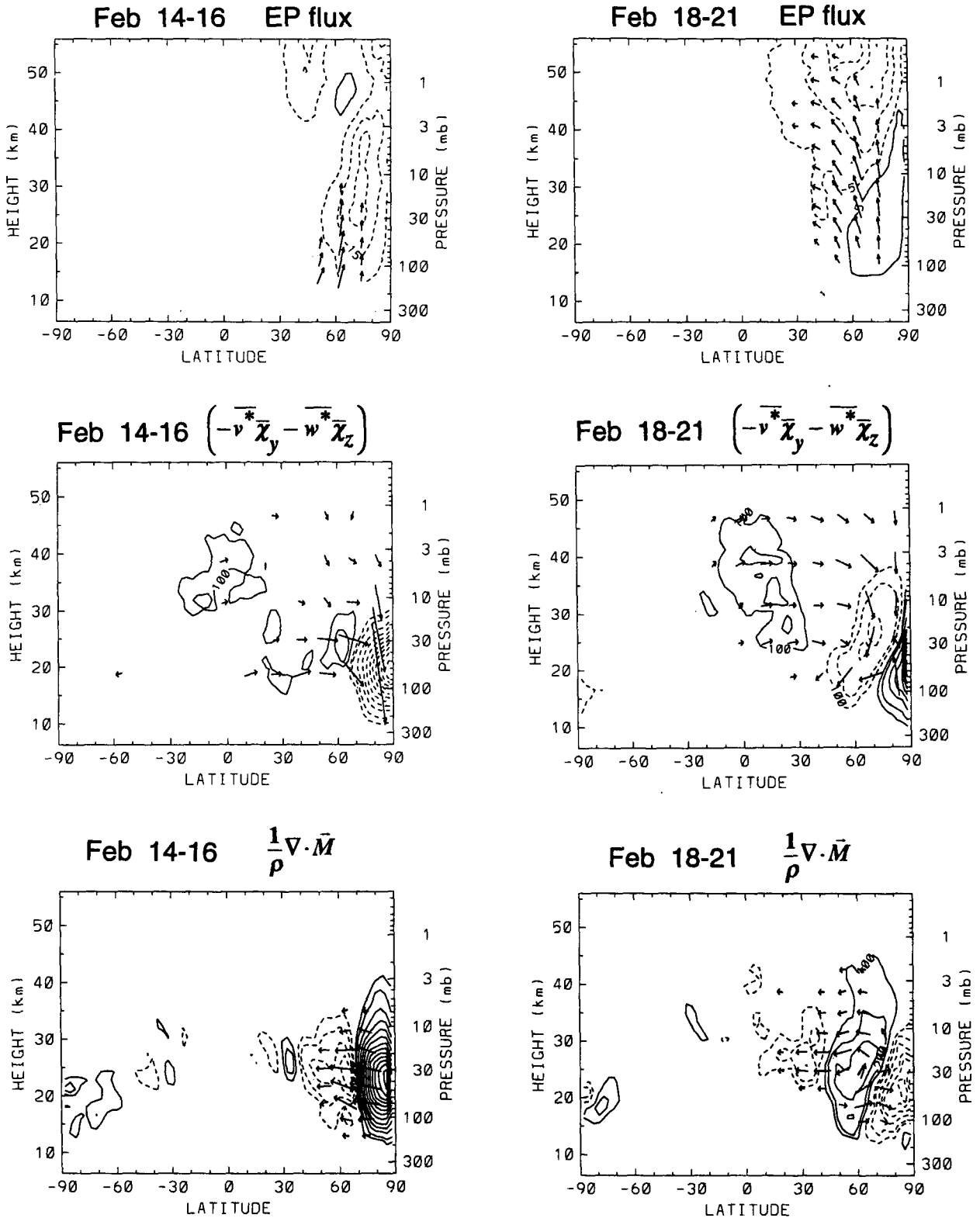
FIG. 12. Signatures of stratospheric wave activity and tracer transport during two phases of a model stratospheric warming event (left and right panels, respectively). Shown are (top) E–P flux vectors and divergence (contours of ±5, 15, ... m s^{-1} day^{-1}), (middle) residual mean circulation vectors (scaled by the square root of density) and tracer advection tendency, and (bottom) eddy tracer flux vectors M and flux divergence tendency. Contours in the lower two panels are ±100, 200, 400 ... ppbv 100 day^{-1}.

shows strong vertical wave propagation in the upper troposphere and lower stratosphere, together with strong eddy N_2O flux in high latitudes over 15–30 km, and intensified downward mean circulation over the polar cap. As time proceeds (right-hand panels in Fig. 12), the wave propagates upward and equatorward in the middle stratosphere. Eddy N_2O fluxes also reach higher altitudes and lower latitudes, while the lower-level polar fluxes (and divergence patterns) reverse sign. Time-average wave N_2O fluxes over this warming event (not shown) are qualitatively similar to the seasonal-average patterns shown in Fig. 8, but substantially stronger. Poleward wave fluxes in the subtropics during this latter phase occur in the form of large-scale "tongues" of tracer advected out of the Tropics, as illustrated in Fig. 13. The character of this tropical–midlatitude transport is in good agreement with CLAES N_2O observations (Randel et al. 1993; Manney et al. 1994) and related subtropical transport simulations (Waugh 1993; Chen and Holton 1994; Polvani et al. 1994). Note also the meridional transport variations over the equator seen in Fig. 12; there is a modulation of the tropical residual circulation associated with winter hemisphere wave forcing [this effect is observed and analyzed in global ozone data in Randel (1993)].

5. Summary and discussion

a. Comparisons with CLAES data

Comparisons between the model-simulated N_2O and CLAES observations show overall good agreement in the middle stratosphere. Seasonal variation of the tropical maximum region is similar, and polar vortex–surf zone structure is well simulated in the model. There is a period of enhanced zonal-mean variability in midlatitudes during early–middle winter in both model and observations, and this accompanies movement of the tropical maximum region toward the summer hemisphere (and tightening of the subtropical gradients in the winter hemisphere). In the upper stratosphere the observations show much stronger seasonality than that found in the model, and this is at least partially due to a relatively weak SAO circulation in the model upper stratosphere.

We have not focused here on detailed model–CLAES N_2O comparisons in the lower stratosphere, or on higher-order statistics (such as wave fluxes) derived from the CLAES data. Our analyses of the Version 6 CLAES data show notable differences from the model simulations for these aspects, and accurate budget analyses based on these data are not possible at present. We plan to extend the comparisons and analyses presented here with future improved versions of the CLAES N_2O and other UARS tracer measurements.

b. Model budget analyses

One utility of GCM simulations is that accurate budget studies can be performed (although care must
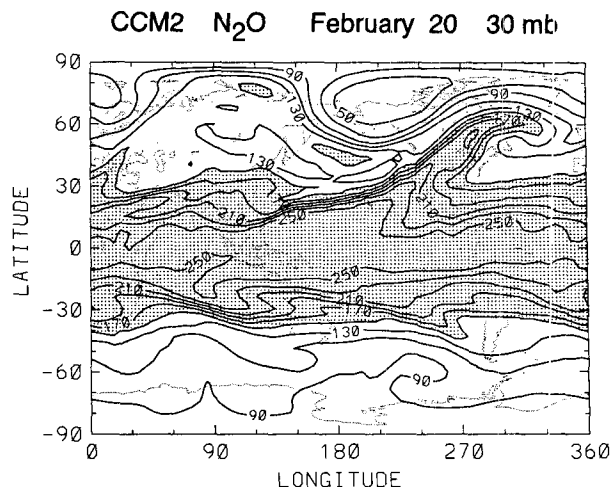

FIG. 13. Instantaneous model N_2O field (ppbv) at 30 mb during the mature phase of the stratospheric warming event.

be taken in some instances to avoid imbalances due to numeric or sampling considerations). Here we have used the daily average output of CCM2 to study the TEM budget of zonal-mean N_2O ($\overline{\chi}$) in the stratosphere and are able to achieve a high degree of balance in these calculations. The seasonal budget analyses presented here focused on the balance of time-averaged quantities during early–middle NH winter (the period of strongest seasonal variation in $\overline{\chi}$). Southward movement of the tropical $\overline{\chi}$ maximum results primarily from mean upward circulation in the summer hemisphere subtropics (increasing local $\overline{\chi}$), combined with the convergence of wave fluxes in the winter hemisphere subtropics (decreasing local $\overline{\chi}$). This result quantifies the importance of planetary wave tracer transport in the winter subtropics and shows that its influence reaches all the way to the equator. The influence of such wave effects in forming and sharpening the subtropical gradient region is similar to the way in which potential vorticity (PV) transport in the surf zone acts to enhance vortex PV gradients. Formation of the winter vortex minimum in $\overline{\chi}$ occurs via a residual of the opposing large effects of mean downward motion and divergence of eddy transports. Also, "filling in" of low $\overline{\chi}$ values in the SH vortex during the spring–summer transition occurs due to the effects of large-scale wave transport.

The daily $\overline{\chi}$ budget in winter extratropics is characterized by the opposing influences of wave transport effects and mean flow advection, with the actual $\overline{\chi}$ tendencies following $\rho^{-1} \nabla \cdot \mathbf{M}$ [this was previously demonstrated in the Eulerian-mean budget analyses of Mahlman et al. (1980)]. There is a high degree of temporal reversibility in the individual budget terms (Fig. 11), so that time means are averages over periods with large compensating effects. Evolution of the balances through a model stratospheric warming event (Fig. 12) shows strong local tendencies that are to some degree

reversible over the life cycle. Wave tracer transport patterns exhibit upward and equatorward movement during the life cycle, qualitatively similar to the upward and equatorward movement observed in E–P flux patterns. Clear tropical transport variations are also observed during these events, resulting from modulation of the global residual circulation. Overall the model simulation is in good agreement with transport aspects of observed stratospheric warming events (Leovy et al. 1985; Randel 1993; Manney et al. 1994); these model budget results will provide a reference for future quantitative budget studies using observed constituent data.

REFERENCES

Andrews, D. G., J. R. Holton, and C. B. Leovy, 1987: *Middle Atmosphere Dynamics.* Academic Press, 489 pp.

Boville, B. A., 1994: Middle atmosphere version of CCM2: Annual cycle and interannual variability. *J. Geophys. Res.,* in press.

Chen, P., and J. R. Holton, 1994: Mass exchange between the Tropics and extratropics in the stratosphere. *J. Atmos. Sci.,* 51, 3006–3018.

Dunkerton, T. J., and D. P. Delisi, 1988: Seasonal variation of the semiannual oscillation. *J. Atmos. Sci.,* 45, 2772–2787.

Edmon, H. J., Jr., B. J. Hoskins, and M. E. McIntyre, 1980: Eliassen–Palm cross sections for the troposphere. *J. Atmos. Sci.,* 37, 2600–2616.

Garcia, R. R., and S. Solomon, 1983: A numerical model of zonally averaged dynamical and chemical structure of the middle atmosphere. *J. Geophys. Res.,* 88, 1379–1400.

——, and B. A. Boville, 1994: "Downward control" of the mean meridional circulation and temperature distribution of the polar winter stratosphere. *J. Atmos. Sci.,* 51, 2238–2245.

——, F. Stordal, S. Solomon, and J. T. Kiehl, 1992: A new numerical model of the middle atmosphere. 1. Dynamics and transport of tropospheric source gasses. *J. Geophys. Res.,* 97, 12 967–12 991.

Gille, J. C., and W. Grose, Eds., 1994: Temperature and constituents. Report of the 1994 Upper Atmosphere Research Satellite Workshop III, NASA Reference Publication.

——, L. V. Lyjak, and A. K. Smith, 1987: The global residual mean circulation in the middle atmosphere for the northern winter period. *J. Atmos. Sci.,* 44, 1437–1452.

Hartmann, D. L., K. R. Chan, B. L. Gary, M. R. Schoeberl, P. A. Newman, R. L. Martin, M. Loewenstein, J. R. Podolske, and S. E. Strahan, 1989: Potential vorticity and mixing in the South Polar vortex during spring. *J. Geophys. Res.,* 94, 11 625–11 640.

Holton, J. R., and W.-K. Choi, 1988: Transport circulation deduced from SAMS trace species data. *J. Atmos. Sci.,* 45, 1929–1939.

Jones, R. L., and J. A. Pyle, 1984: Observations of CH_4 and N_2O by the NIMBUS 7 SAMS: A comparison with in-situ data and two-dimensional numerical model calculations. *J. Geophys. Res.,* 89, 5263–5279.

Kumer, J. B., J. L. Mergenthaler, and A. E. Roche, 1993: CLAES CH_4, N_2O and $CCl_2F_2(F_{12})$ global data. *Geophys. Res. Lett.,* 20, 1239–1242.

Leovy, C. B., C.-R. Sun, M. H. Hitchman, E. E. Remsberg, J. M. Russell III, L. L. Gordley, J. C. Gille, and L. V. Lyjak, 1985: Transport of ozone in the middle stratosphere: Evidence for planetary wave breaking. *J. Atmos. Sci.,* 42, 230–244.

Mahlman, J. D., and L. J. Umscheid, 1987: Comprehensive modeling of the middle atmosphere: The influence of horizontal resolution. *Transport Processes in the Middle Atmosphere,* G. Visconti and R. Garcia, Eds., Reidel, 485 pp.

——, H. Levy II, and W. J. Moxim, 1980: Three-dimensional tracer structure and behavior as simulated in two ozone precursor experiments. *J. Atmos. Sci.,* 37, 655–685.

——, ——, and ——, 1986: Three-dimensional simulations of stratospheric N_2O: Predictions for other trace constituents. *J. Geophys. Res.,* 91, 2687–2707.

Manney, G. L., R. W. Zurek, A. O'Neill, R. Swinbank, J. B. Kumer, J. L. Mergenthaler, and A. E. Roche, 1994: Stratospheric warmings during February and March 1993. *Geophys. Res. Lett.,* 21, 813–816.

Polvani, L. M., D. W. Waugh, and R. A. Plumb, 1994: On the subtropical edge of the stratospheric surf zone. *J. Atmos. Sci.,* submitted.

Prather, M., and E. Remsberg, Eds., 1992: The atmospheric effects of stratospheric aircraft. Report of the 1992 models and measurements workshop, NASA Reference Publication 1292 (NASA 1292), 268 pp.

Randel, W. J., 1993: Global variations of zonal mean ozone during stratospheric warming events. *J. Atmos. Sci.,* 50, 3308–3321.

——, J. C. Gille, A. E. Roche, J. B. Kumer, J. L. Mergenthaler, J. W. Waters, E. F. Fishbein, and W. A. Lahoz, 1993: Stratospheric transport from the tropics to middle latitudes by planetary wave mixing. *Nature,* 365, 533–535.

Russell, J. M., III, A. F. Tuck, L. L. Gordley, J. H. Park, S. R. Drayson, J. E. Harries, R. J. Cicerone, and P. J. Crutzen, 1993: HALOE Antarctic observations in the spring of 1991. *Geophys. Res. Lett.,* 20, 719–722.

Sassi, F., R. R. Garcia, and B. A. Boville, 1993: The stratopause semiannual oscillation in the NCAR Community Climate Model. *J. Atmos. Sci.,* 50, 3608–3624.

Schoeberl, M. R., L. R. Lait, P. A. Newman, and J. E. Rosenfield, 1992: The structure of the polar vortex. *J. Geophys. Res.,* 97, 7859–7882.

Solomon, S., J. T. Kiehl, R. R. Garcia, and W. Grose, 1986: Tracer transport by the diabatic circulation deduced from satellite observations. *J. Atmos. Sci.,* 43, 1603–1617.

Stanford, J. L., J. R. Ziemke, and S. Y. Gao, 1993: Stratospheric circulation features deduced from SAMS constituent data. *J. Atmos. Sci.,* 50, 226–246.

Strahan, S. E., and J. D. Mahlman, 1994: Evaluation of the SKYHI general circulation model using aircraft N_2O measurements. 1. Polar winter stratospheric meteorology and tracer morphology. *J. Geophys. Res.,* 99, 10 305–10 318.

Waugh, D., 1993: Subtropical stratospheric mixing linked to disturbances in the polar vortices. *Nature,* 365, 535–537.